Inference of Marine Stratus Cloud Optical Depths from Satellite Measurements: Does 1D Theory Apply?

NORMAN G. LOEB* AND J. A. COAKLEY JR.

College of Oceanic and Atmospheric Sciences, Oregon State University, Corvallis, Oregon

(Manuscript received 4 November 1996, in final form 17 March 1997)

ABSTRACT

The validity of plane-parallel (1D) radiative transfer theory for cloudy atmospheres is examined by directly comparing calculated and observed visible reflectances for one month of Global Area Coverage Advanced Very High Resolution Radiometer satellite observations of marine stratus cloud layers off the coasts of California, Peru, and Angola. Marine stratus are an excellent testbed, as they arguably are the closest to plane-parallel found in nature. Optical depths in a 1D radiative transfer model are adjusted so that 1D model reflectances match those observed at nadir on a pixel-by-pixel basis. The 1D cloud optical depth distributions are then used in the plane-parallel model to generate reflectance distributions for different sun–earth–satellite viewing geometries. These reflectance distributions are directly compared with the observations. Separate analyses are performed for overcast and broken cloud layers as identified by the spatial coherence method.

When 1D reflectances are directly compared with observations at different view angles, relative differences are generally small ($\lesssim$10%) in the backscattering direction for solar zenith angles $\lesssim 60^\circ$ and show no systematic view angle dependence. In contrast, 1D reflectances increase much more rapidly with view angle than the observed reflectances in the forward-scattering direction. Relative differences in the forward-scattering direction are $\approx$2–3 times larger than in the backscattering direction. At solar zenith angles $\gtrsim 60^\circ$, the 1D model underestimates observed reflectances at nadir by 20%–30% and overestimates reflectances at the most oblique view angles in the forward scattering direction by 15%–20%. Consequently, when inferred on a pixel-by-pixel basis, nadir-derived cloud optical depths show a systematic increase with solar zenith angle, both for overcast and broken cloud layers, and cloud optical depths decrease with view angle in the forward scattering direction. Interestingly, in the case of broken marine stratocumulus, the common practice of assuming that pixels are overcast when they are not mitigates this bias to some extent, thereby confounding its detection. But even for broken clouds, the bias remains.

Because of the nonlinear dependence of cloud albedo on cloud optical depth, errors in cloud optical depth lead to large errors in cloud albedo—and therefore energy budget calculations—regardless of whether cloud layers are overcast or broken. These findings suggest that as a minimum requirement, direct application of the plane-parallel model approximation should be restricted to moderate–high sun elevations and to view angles in the backscattering direction. Based on Monte Carlo simulations, the likely reason for the discrepancies between observed radiances and radiances calculated on the basis of 1D theory is because real clouds have inhomogeneous (i.e., bumpy) tops.

1. Introduction

Common practice in the remote sensing of cloud properties and radiative flux calculations is to use the plane-parallel approximation, which assumes clouds to be one-dimensional and therefore horizontally invariant. While numerous theoretical studies over the past 20 yr have shown that 3D and 1D clouds reflect radiation very differently (e.g., Busygin 1973; McKee and Cox 1974; Wendling 1977; Davies 1978, 1984; Bréon 1992; Kobayashi 1993; Barker 1994; Loeb et al. 1997; Loeb et al. 1998, manuscript submitted to *J. Atmos. Sci*), only a handful of studies have examined this problem observationally (e.g., Stuhlmann et al. 1985; Coakley and Davies 1986; Coakley 1991; Davies 1994; Loeb and Davies 1996, 1997). Given that satellite observations are routinely used to infer global cloud properties from which radiative fluxes at the top of the atmosphere, within the atmosphere, and at the surface are calculated, it is essential that the limitations of the 1D approach be well understood.

Previously, Loeb and Davies (1996, 1997) showed that for the general cloud scene over the ocean, significant differences between observed and 1D reflectances can result—especially in the reflectance dependence on solar zenith angle. Those studies were based on 1 yr of Earth Radiation Budget Experiment (ERBE) scanner ob-

* Current affiliation: Center for Atmospheric Sciences, Hampton University, Hampton, Virginia.

Corresponding author address: Dr. Norman G. Loeb, Mail Stop 420, NASA Langley Research Center, Hampton, VA 23681.

TABLE 1. Orbit, number of days, solar zenith angle (θ_0) range, and approximate local time for each region and satellite. ''A'' = ascending orbit; ''D'' = descending orbit. *NOAA-11* observations are from June 1994, while *NOAA-12* and *NOAA-14* are from June 1995 (for Angola, June 1995 observations were supplemented by May 1995 data).

Region	Satellite	Orbit	Number of days	θ_0 Range	Local time
Peru	*NOAA–11*	A	20	77°–90°	1700
5°–30°S	*NOAA–12*	D	30	75°–90°	0658
70°–95°W	*NOAA–14*	A	22	38°–63°	1354
Angola	*NOAA–11*	A	28	76°–86°	1656
5°–20°S	*NOAA–12*	D	27	75°–87°	0701
15°–15°E	*NOAA–14*	A	43	38°–53°	1352
California	*NOAA–11*	A	22	55°–62°	1623
25°–40°N	*NOAA–11*	D	27	81°–91°	0512
115°–140°W	*NOAA–12*	D	28	56°–62°	0732
	NOAA–14	A	28	19°–25°	1319

servations, which are broadband and have a low spatial resolution (31×47 km^2 at nadir). In the present study, a very similar analysis is performed using one month of *NOAA-11*, *-12*, and *-14* Global Area Coverage (GAC) Advanced Very High Resolution Radiometer (AVHRR) (Kidwell 1994) measurements off the coasts of Peru, Angola, and California. The analysis is now restricted to layered marine clouds. Since these clouds tend to frequently occur in single layers, contain only water droplets, have low aspect ratios, and have relatively uniform cloud tops, they are arguably the closest to plane parallel found in nature and are therefore an excellent testbed for examining the suitability of 1D theory in analyzing satellite measurements of clouds.

The aim here is to identify sun–earth–satellite viewing conditions for which the 1D model assumption appears to be consistent with observations as well as conditions for which 1D theory leads to biases in retrieved cloud optical depth and hence cloud albedo. Note that the absolute accuracy of 1D cloud optical depth retrievals are not being evaluated here, as this would require measurements of the optical depths by independent means (e.g., measurements of column amounts of cloud liquid water and droplet radii). Rather, it is the consistency of the retrievals for different viewing geometries that is examined. Cloud optical depths inferred for different viewing geometries are compared with those obtained at nadir and high sun (used as the reference throughout this study). For viewing geometries where inconsistencies occur, quantitative estimates of the biases are provided, both in terms of cloud optical depth and cloud albedo.

In the following sections, the observations and methodology are described, and a detailed error analysis is provided. The comparisons include a direct comparison between observed and 1D model reflectances over a wide range of viewing geometries, a test of the consistency of 1D model retrievals of cloud optical depth, and the consistency of top-of-the-atmosphere (TOA) albedos calculated from the cloud optical depth retrievals for the range of observed viewing angles. In order to examine whether these comparisons further depend on whether overcast or broken clouds are considered, separate comparisons are performed for observations that are overcast at the pixel scale and for observations in which the pixels are simply cloud contaminated. Scene identification is performed using the spatial coherence method of Coakley and Bretherton (1982).

2. Observations

Observed reflectance $R(\tau_p; \mu, \mu_o, \phi)$ (or equivalently, isotropic albedo) is inferred from Global Area Coverage (GAC) Advanced Very High Resolution Radiometer (AVHRR) channel 1 (0.63 μm) measurements as follows:

$$R(\tau_p; \mu, \mu_o, \phi) = \frac{\pi I(\tau_p; \mu, \mu_o, \phi)}{\mu_o F} \times 100\%, \quad (1)$$

where I = pixel radiance (W m^{-2} sr^{-1} μm^{-1}), F = solar irradiance (W m^{-2} μm^{-1}), τ_p = cloud optical depth, μ = cosine of observer zenith angle, μ_o = cosine of solar zenith angle, and ϕ = azimuth angle relative to the solar plane ($\phi = 0°$ corresponds to forward scattering).

One month of AVHRR *NOAA-11*, *-12*, and *-14* measurements over ocean regions off the coasts of Peru, Angola, and California are considered. The NOAA satellites fly in a sun-synchronous orbit with morning (*NOAA-12*) and afternoon (*NOAA-11* and *NOAA-14*) equator crossing times. To ensure AVHRR measurements on the different NOAA satellites are well calibrated, a new in-flight calibration technique is used that takes advantage of the spatial and temporal stability of ice surfaces over Greenland and Antarctica (Loeb 1997).

Table 1 provides the number of days, the solar zenith angle range (θ_o) corresponding to the nadir view, and the approximate local time of the satellite overpasses for each region. The *NOAA-11* observations correspond to June 1994, and the *NOAA-12* and *NOAA-14* data to June 1995 (over Angola, *NOAA-14* June 1995 observations were supplemented by observations for May 1995). Observations from different NOAA satellites and different geographical regions were used in order to increase the range of sun–earth–satellite viewing ge-

ometries available for comparing 1D theory with observations. Observations from California, Angola, and Peru were selected because each of these regions has a high frequency of marine stratus (Warren et al. 1988).

GAC AVHRR data is produced from the intrinsic 1.1-km observations by averaging along-scan groups of four samples out of five and using every third scan (Kidwell 1994). With this sampling, a nadir GAC pixel is interpreted as representing an area of $\sim(4\ \text{km})^2$. There are 409 pixels along a scan line with zenith angles ranging from 0° to 70° on each side. For the intrinsic 1.1-km observations, pixel area increases with view angle by a factor of ≈12 from nadir to the limb (Singh and Cracknell 1986; Frulla et al. 1995). Thus, a GAC pixel reaches a size of $\sim(14\ \text{km})^2$ at the most oblique view. To ensure that this, and other factors such as regional differences and diurnal effects, do not compromise the results through sampling biases, a detailed error analysis is provided in section 4.

In this study, the observations are stratified into 10 intervals of μ_o between 0 and 1, 7 intervals of μ between 0.3 and 1, and 18 intervals of ϕ of width 10° between 0° and 180° (symmetry about the solar plane is assumed). For the most oblique μ bin, only observations at view angles for which the cosine is between 0.34 and 0.4 are available. The spatial resolution of a pixel at the midpoint of this bin is $\sim(13\ \text{km})^2$.

3. Methodology

The approach used to compare observed and 1D reflectances closely follows that of Loeb and Davies (1996, 1997). Optical depths (τ_p) are adjusted in 1D calculations of reflectance so that the model and observed nadir reflectances match on a pixel-by-pixel basis. Distributions of τ_p are then used in the 1D model to generate reflectance distributions for different sun–earth–satellite geometries. These reflectances are directly compared with the observed reflectances. To examine the influence of broken clouds on cloud anisotropy, separate analyses are performed for pixels identified as being completely cloud filled (i.e., overcast), and pixels that are cloud contaminated but not necessarily overcast. These distinctions are determined using the spatial coherence method (Coakley and Bretherton 1982). To ensure that cloud-free pixels are excluded from these analyses, only observations with $\tau_p \geq 1$ are considered. Note that τ_p distributions for the partly cloudy pixels are inferred in the same manner as for the overcast pixels—that is, the pixels are assumed to be completely cloud filled. This assumption is also used by the International Satellite Cloud Climatology Project (ISCCP) to infer cloud optical properties from cloud-contaminated pixels (Rossow 1989).

To ensure that the results are general, and not influenced by the choice of model assumptions, comparisons are performed using a wide range of model inputs. Three different effective radii (r_e), 6, 10, and 20 μm, are used. The standard calculations are for a cloud with a top height of 1 km embedded in a marine tropical atmosphere (Kneizys et al. 1988). Calculations are also performed in which scattering and absorption by atmospheric gases and aerosols are ignored.

As demonstrated in section 4c, and from many studies in the literature (Minnis and Harrison 1984; Minnis et al. 1992), diurnal effects can be substantial in regions containing stratus. To avoid biases due to diurnal effects, separate analyses are performed for the morning (*NOAA-12*) and afternoon (*NOAA-11, -14*) satellite measurements.

a. Identification of overcast fields of view

The spatial coherence method (SCM) of Coakley and Bretherton (1982) is used for scene identification. For layered cloud systems that extend over moderately large regions $>(250\ \text{km})^2$ with completely clear and cloudy pixels spanning several fields of view, the method utilizes the spatial structure of the IR radiance field to distinguish between clear, completely cloud covered, and partially filled fields of view. Coakley and Bretherton (1982) showed that when infrared radiance standard deviations over localized regions are plotted against mean radiances, a characteristic pattern is observed, whereby cloud-free and overcast areas form separate, well-defined clusters or ''feet'' of arches in which low values of the standard deviation at different brightness temperatures occur. Partly cloud-filled regions show considerable scatter and higher standard deviations, with brightness temperatures falling between clear and overcast values. When a single arch-like structure is observed, the method assumes that the clouds are in a single layer and are optically thick at the wavelength of observation, 11 μm.

Here, scenes are subdivided into frames of 68 scan spots by 64 scan lines representing an area of $(264\ \text{km})^2$ at nadir. Means and standard deviations for 2×2 pixel arrays of GAC data are calculated within each frame (i.e., a total 34×32 pixel arrays) to determine which elements belong to the feet of an arch and which do not. Next, pixels within subframes of 34 scan spots by 16 scan lines $\sim(90\ \text{km})^2$ are examined to determine which pixels belong to a particular foot. A detailed description of this analysis is provided in Coakley and Baldwin (1984; section 3a) for slightly different frame and subframe sizes.

b. Plane-parallel model calculations

Lookup tables of cloud reflectance are generated as a function of viewing geometry using the DISORT program of Stamnes et al. (1988), which is based on the discrete ordinates method. The lookup tables consist of cloud reflectances determined at 24 cloud optical depths (defined at 0.55 μm) between 0.5 and 200, 18 view and solar zenith angles between 0° and 89°, and 19 relative

azimuth angles between 0° and 180°. Forty-eight streams are used in the calculations, and a correction for earth curvature effects is included. The atmosphere is divided into four homogeneous layers consisting of a boundary layer, a cloud layer, a tropospheric layer, and a stratospheric layer. Ocean surface reflectance below the cloud layer is assumed to be Lambertian with an albedo of 7%. As mentioned earlier, two assumptions regarding cloud-top height are considered. For the standard case, a constant cloud-top height of 1 km is assumed. This altitude corresponds to the base height of the temperature inversion typically observed for stratus clouds off the coast of California (Klein and Hartmann 1993). For a second set of calculations, scattering and absorption by gases and aerosols in the atmosphere are removed.

When present, scattering above/below the cloud layer by the atmosphere is modeled using optical properties from the LOWTRAN-7 model (Kneizys et al. 1988). For the 0.63-μm AVHRR channel, the principle influence by the atmosphere on radiation reflected upward from the cloud involves absorption by O_3 and H_2O and attenuation due to scattering by molecules and aerosols. A maritime aerosol model with a clear-sky vertical optical depth of 0.1 (at a wavelength of 0.5 μm) is assumed. Sensor weighted reflectances are calculated by integrating the sensor response function over nine monochromatic reflectance calculations within the 0.63-μm band (0.5–0.8 μm). To reduce computation times, the *NOAA-11* sensor response function is used for all satellites. Since both transmission and cloud reflectance are reasonably constant with wavelength across the 0.63-μm band, small differences in the sensor response function for the different satellites have negligible effects.

Within the cloud, the standard case takes droplet sizes to be given by a gamma distribution of water spheres with an effective radius of 10 μm. This distribution is the same as that used by ISCCP (Rossow et al. 1989). For comparison, two modified gamma distributions (Deirmendjian 1969) with effective radii of 6 and 20 μm are also used. Single scattering properties are calculated using the Mie code of Bohren and Huffman (1983) and the refractive indices of Hale and Querry (1973).

4. Error analysis

Uncertainties in mean reflectance are determined from the standard error in the mean at the 95% significance level. In order to reduce uncertainties due to temporal and spatial autocorrelation between pixel measurements within an image, mean reflectances and standard deviations in each angular bin are inferred from daily means. Thus, daily mean reflectances are assumed independent.

The following describes estimates of systematic errors in the observed reflectances that may arise due to changes in pixel resolution with view angle, differences in the cloud properties for the different regions, and the diurnal variations of the cloud properties.

a. Pixel resolution

As noted in section 2, pixel resolution changes from ~4 km at nadir to ~13 km at the midpoint of the most oblique view-angle bin. Because the infrared radiance variance across 2 × 2 pixel arrays decreases with decreasing pixel resolution (Coakley and Bretherton 1982; Wielicki and Welch 1986), the SCM may be less sensitive to subpixel breaks in the cloud field at the limb than at nadir. Consequently, errors in identification of overcast pixels are expected to increase with increasing view angle. This will cause errors in reflectance associated with overcast pixels to also increase with view angle. Here, a quantitative estimate of the relative uncertainty in reflectance due to changes in pixel resolution with view angle is provided. Errors in reflectance are estimated by comparing overcast near-nadir pixel reflectances at full and degraded resolutions. Reflectances at degraded pixel resolutions are obtained by averaging over an appropriate number of neighboring nadir GAC pixels whose combined area matches the area of pixels at the off-nadir view angles. After averaging nadir pixels to obtain reflectances for a given pixel resolution, the SCM is applied, and the reflectance uncertainty is estimated from the difference between the degraded- and full-resolution (4 km) mean nadir reflectance.

Two degraded pixel resolutions are considered: (8 km)^2, corresponding to the area at $\mu \approx 0.57$; and (11 km)^2, corresponding to the area at $\mu \approx 0.42$. The (8-km)^2 pixels were constructed by averaging two along-track and two cross-track GAC nadir pixels, while the (11-km)^2 pixels were generated using four along-track and two cross-track GAC nadir pixels. For each image (or day) throughout the month, the SCM is run at 4-, 8-, and 11-km resolutions. Then, considering only pixels with $\mu > 0.9$, the frequency of overcast pixels is inferred from the ratio of the number of pixels flagged as overcast to the total number of nadir pixels. The corresponding mean reflectance for the overcast pixels at each resolution is also calculated and results for the full and degraded pixel resolutions are compared directly.

Figures 1a and 1b show scatterplots of degraded- and full-resolution overcast reflectance for 8- (Fig. 1a) and 11-km (Fig. 1b) pixels. Each point represents an average reflectance over the same scene (one scene per day) at the two resolutions. Included are all images with $\mu_o > 0.4$ (i.e., all *NOAA-14* and the California *NOAA-11*A and *NOAA-12*D orbits). As shown, reflectances from degraded resolution pixels tend to be lower than those obtained at full resolution. This difference is more pronounced at the 11-km resolution than at 8 km. Figures 2a and 2b show the corresponding frequencies of occurrence for overcast pixels. Unlike the results for the reflectances, the frequencies of occurrence for the full

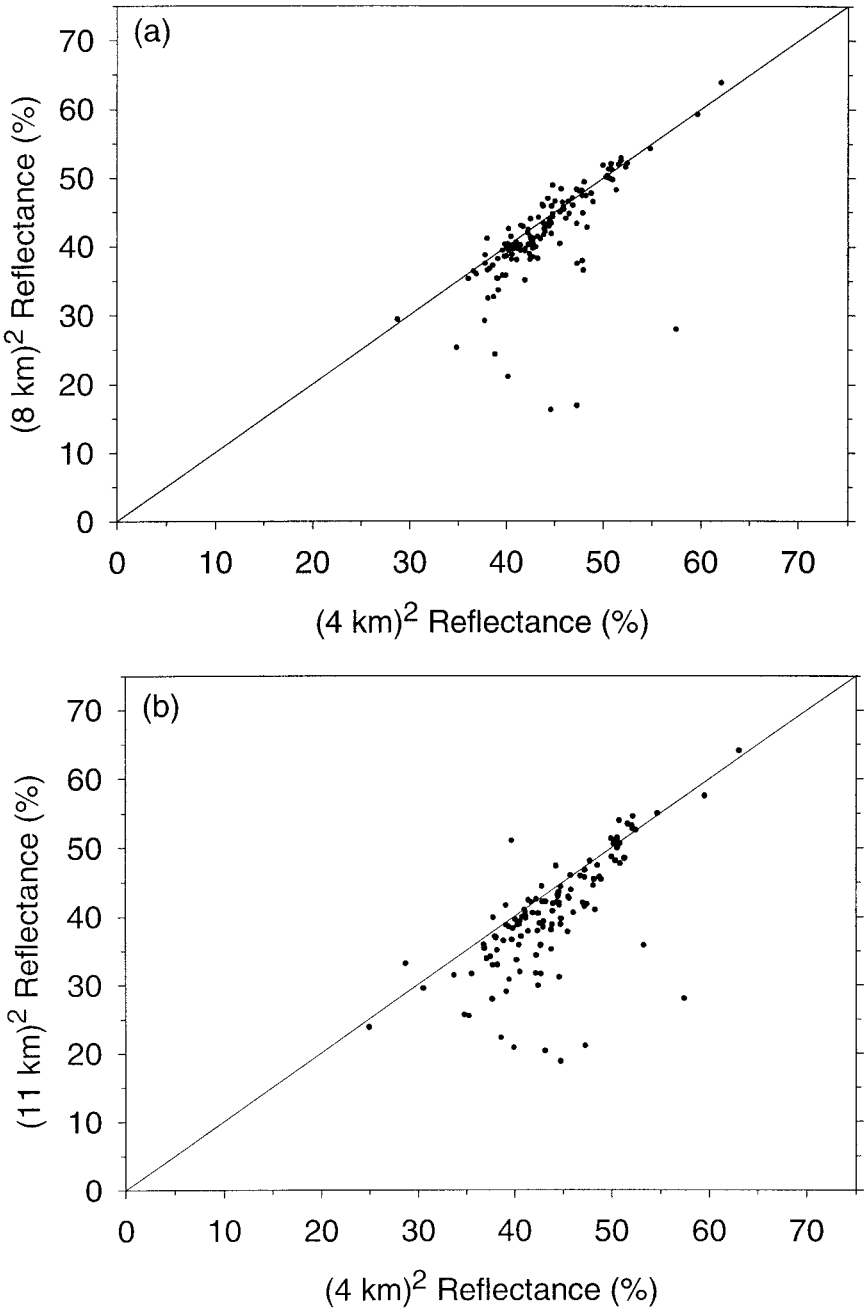

FIG. 1. Degraded- and full-resolution overcast nadir reflectances for degraded pixel resolutions of (a) 8 km and (b) 11 km. Full-resolution pixel is 4 km (GAC). Each point represents an average reflectance over the same scene (one scene per day) at the two resolutions. Included are all images with $\mu_o > 0.4$ (133 cases).

and degraded resolutions do not appear to show any systematic difference, despite the large scatter at high values of the frequency of occurrence. With a perfect method of scene identification, the frequency of overcast pixels would be expected to decrease with increasing pixel area (Shenk and Salomonson 1972; Wielicki and Parker 1992; Ye and Coakley 1996; Di Girolamo and Davies 1997), and the overcast cloud reflectance would remain constant. Since the results in Figs. 1 and 2 fail to show such trends, the SCM evidently loses sensitivity with increasing pixel resolution.

Table 2 provides a summary of the mean nadir reflectance and frequency of overcast pixels as a function of pixel resolution. As noted above, the overcast pixel frequency of occurrence is relatively insensitive to pixel resolution—in all three cases, the average frequency of

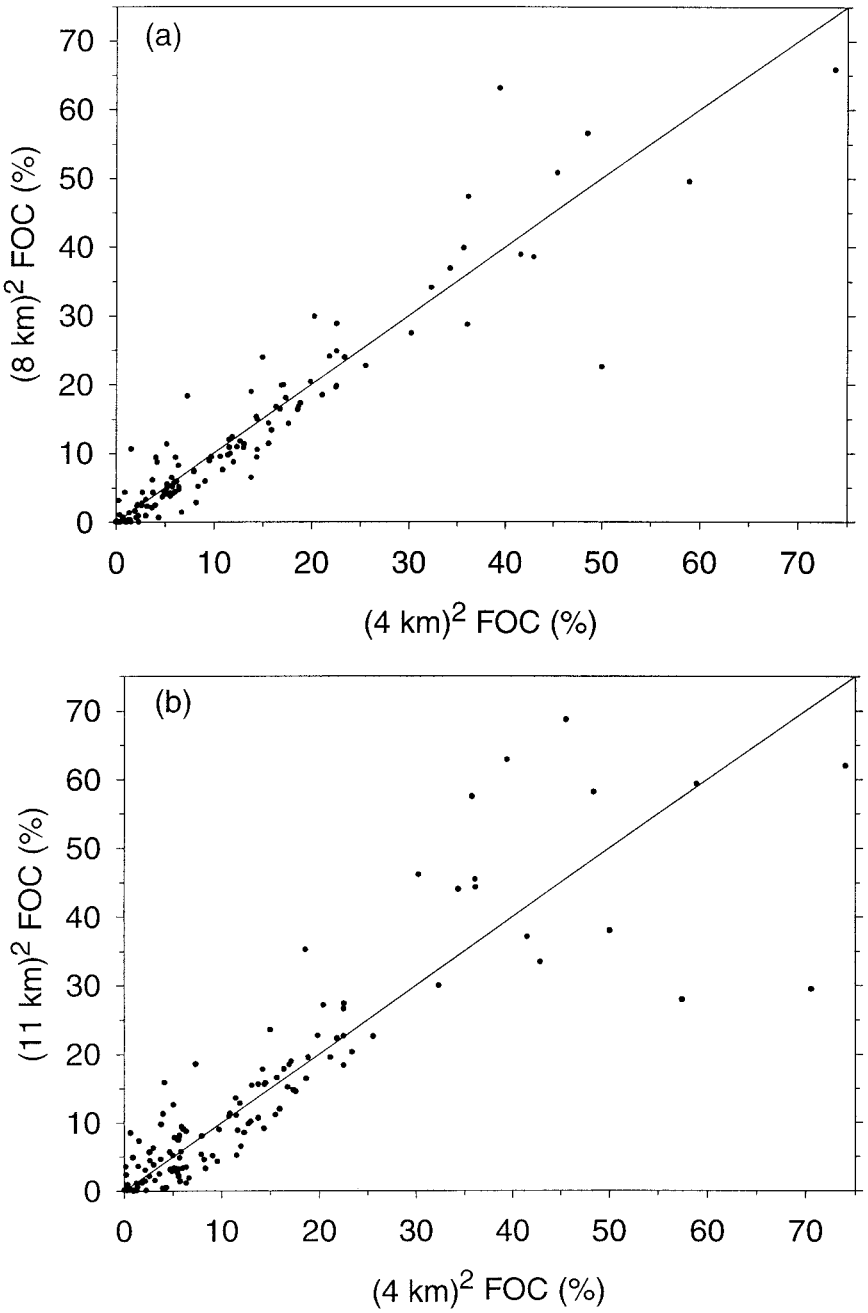

FIG. 2. Degraded- and full-resolution frequencies of occurrence (FOC) for overcast pixels at nadir for degraded pixel resolutions of (a) 8 km and (b) 11 km. Full-resolution pixel is 4 km (GAC).

overcast pixels is ≈12%. When observations at other view angles are examined, a similar trend is observed. Figure 3 shows the frequency of overcast pixels at different μ for the same scenes. Error bars are given by the standard error in the mean at the 95% significance level. As is done in Fig. 3 and all subsequent figures, curves—in this case a cubic spline—are fit to the data points to illustrate the trends in the data. The frequency of overcast pixels, as shown in Fig. 3, remains between ≈10%–15% at all μ, in agreement with the nadir results.

In contrast, the mean nadir reflectances in Table 2 show a systematic decrease with increasing pixel size. At full resolution, the mean reflectance is 43.1%, compared to 41.7% at 8 km and 40.0% at 11 km. These correspond to relative differences of ≈3% and ≈7%, respectively, and rms differences of 4.8% and 6.5%. For

TABLE 2. Average (%), standard error (%), and count (number of images) for the mean scene nadir reflectance and overcast pixel frequency of occurrence at 4-, 8-, and 11-km pixel resolutions.

	4-km resolution		8-km resolution		11-km resolution	
	Scene reflectance	Overcast pixel frequency	Scene reflectance	Overcast pixel frequency	Scene reflectance	Overcast pixel frequency
Average	43.1	12.4	41.7	12.2	40.0	12.8
Error	0.6	1.2	0.7	1.3	0.7	1.3
Count	130	131	126	131	123	131

the most oblique μ bin considered here (midpoint at $\mu = 0.37$), the pixel size is slightly larger (13 km). To estimate the uncertainty for this bin, reflectance uncertainties for the 8- and 11-km pixel resolutions are extrapolated to obtain a value of ≈10% at $\mu = 0.37$ for a 13-km pixel. In Table 3, a summary of the reflectance uncertainty estimates for each μ bin is provided. These uncertainties are accounted for (along with the standard error in the mean) in all estimates of the uncertainties.

b. Regional differences

Because clouds tend to be more broken closer to coastlines, the frequency of overcast pixels may also depend on location. Figure 4 shows the frequency of overcast pixels at different μ for *NOAA-11, -14* (''Aft''), and *NOAA-12* (''Morn'') observations in the forward (''Fwd'') and backward (''Bwd'') scattering directions. The viewing directions for the ''Aft Fwd'' and ''Morn Bwd'' cases are always away from the coastline (''AC''), while they are toward the coast (''TC'') for the Aft Bwd and Morn Fwd cases. As shown, the overcast frequency in each orbit (morning/afternoon) tends to be lower when pixels are located closer to the coast (TC), especially during the morning. Therefore, to avoid any misinterpretations of the results due to biases associated with this or any other related effect (e.g., changes in cloud thickness), conclusions reached on the basis of data collected for the afternoon orbits (i.e., *NOAA-11*A, *-14*A) will be verified by repeating the comparisons using data collected for the morning orbit (i.e., *NOAA-12*D).

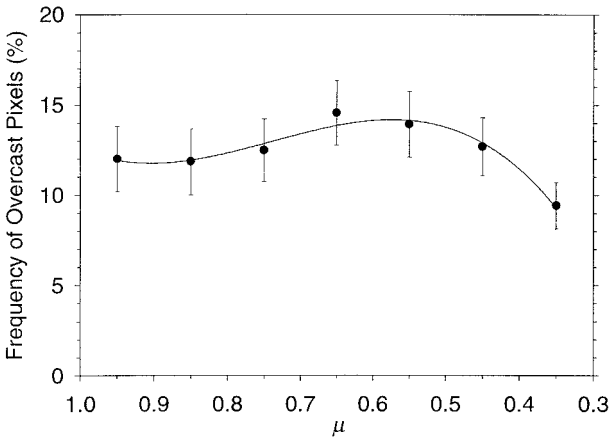

FIG. 3. Frequencies of occurrence for overcast pixels and cosine of the satellite zenith angle, μ, for cosines of the solar zenith angle, μ_o, > 0.4.

In order to ensure that reflectance populations from the three different regions are consistent, mean reflectances from each region are compared directly. Figure 5a shows mean overcast cloud reflectances as a function of μ for observations from Peru and Angola at μ_o = 0.2–0.3 and ϕ = 30°–40° from *NOAA-11*, and Fig. 5b shows results for μ_o = 0.7–0.8 and ϕ = 60°–80° from *NOAA-14*. As shown, the mean reflectance dependence on μ is very similar for both low and moderate sun elevations, and relative differences are everywhere less than ≈5% [where the relative difference between two quantities A and B is defined by $(A - B)/B \times 100\%$]. Comparisons between measurements for the California and Angola (or Peru) regions are limited, however, because the angular coverage for California is quite different from that for the other two regions. The only sun–earth–satellite geometry that is common to all three regions is μ_o = 0.5–0.6 at near-nadir view angles. For that case, the mean reflectances are 41.08% for California (*NOAA-11*), 42.06% for Peru (*NOAA-14*), and 41.58% for Angola (*NOAA-14*). When the above comparisons were repeated using two nonparametric statistical tests—the Wilcoxon Rank-Sum Test and the Cramer–von Mises Test (Sprent 1989)—no differences at the 95% significance level were found between any of the reflectance populations. Thus, as far as can be discerned from the available measurements, there appear to be no systematic differences between the cloud re-

TABLE 3. Approximate pixel area and relative error in mean reflectance due to pixel–area expansion with view angle for the midpoint of each μ bin considered in this study.

μ	Approximate pixel area	Relative error (%)
0.37	(13 km)^2	10
0.45	(11.3 km)^2	7
0.55	(8 km)^2	3
0.65	(6.8 km)^2	2
0.75	(5.7 km)^2	1
0.85	(4.8 km)^2	0.5
0.95	(4 km)^2	0

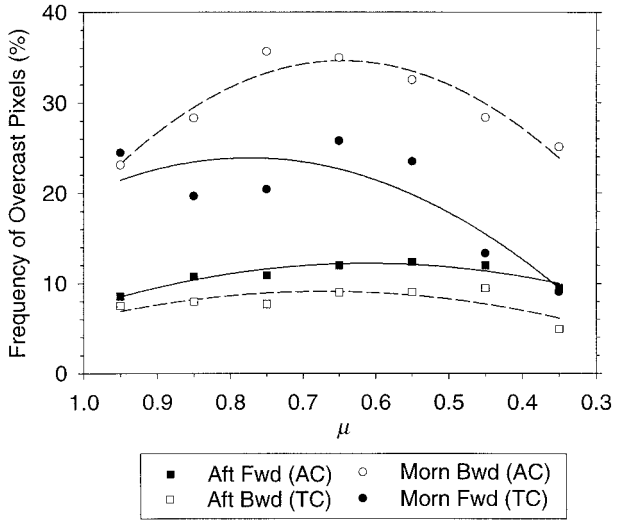

FIG. 4. Frequencies of occurrence for overcast pixels and μ in the forward- (Fwd) and backward- (Bwd) scattering directions from the *NOAA-11, -14* (Aft), and *NOAA-12* (Morn) satellites ($\mu_o > 0.4$). AC = viewing direction is away from the coastline; TC = viewing direction is toward the coastline.

flectances for the three regions. Further, since no significant differences were found between the *NOAA-11* measurements for California and the *NOAA-14* reflectances for Peru and Angola, the uncertainties due to errors in the calibration of *NOAA-11* and *NOAA-14* are likely to be small.

c. Diurnal variations

Figure 6 shows a comparison between observed mean overcast cloud reflectances for the California region using *NOAA-11* (≈1620 LST) and *NOAA-12* (≈0730 LST) observations for and $\mu_o = 0.6$–0.7 and $\phi = 10°$–$30°$. In this case, the *NOAA-12* morning reflectances are significantly larger than the *NOAA-11* afternoon values (at the 95% significance level). By performing separate analyses for the morning and afternoon satellites, uncertainties due to strong diurnal variations are avoided. The only remaining potential uncertainty due to diurnal effects arises from differences between observations at ≈1300 LST (*NOAA-14*) and ≈1700 LST (*NOAA-11*). Using observations from stratus layers near San Nicolas Island, just off the coast of California, during the First International Satellite Cloud Climatology Project (ISCCP) Research Experiment (FIRE), Minnis et al. (1992, Fig. 5) found large decreases in cloud optical depths during the morning hours but much smaller decreases during the afternoon hours. Similarly, using measurements of stratus over the eastern Pacific Ocean (at 21.4°S, 86.3°W), Minnis and Harrison (1984) found fairly similar cloud amounts and cloud-top temperatures between 1300 and 1700 LST (see their Fig. 8). These results, together with those in section 4.2 between *NOAA-11* (California) and *NOAA-14* (Peru and Angola)

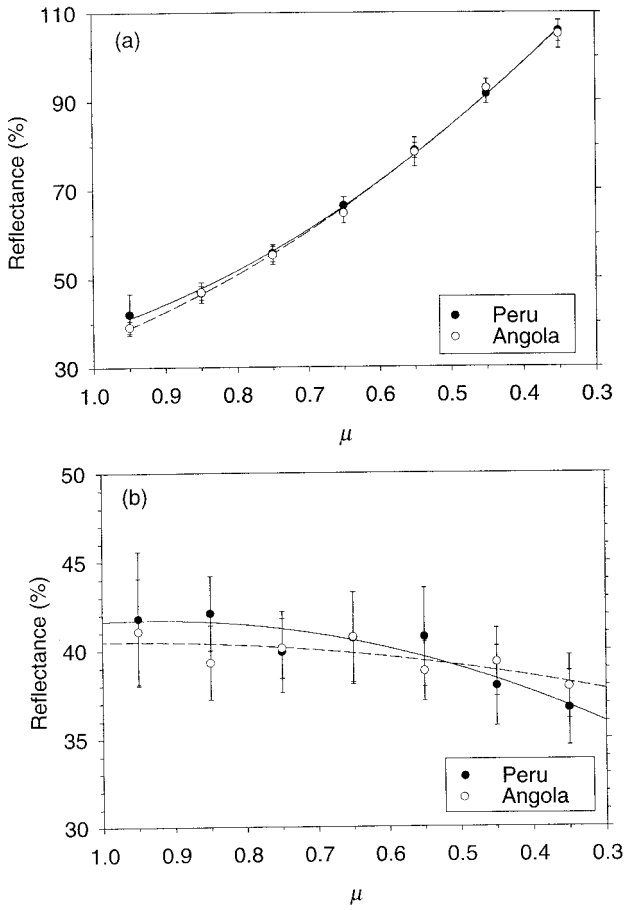

FIG. 5. Mean overcast cloud reflectances and μ for observations off the coasts of Peru and Angola at (a) $\mu_o = 0.2$–0.3 and $\phi = 30°$–$40°$ from *NOAA-11*; and (b) $\mu_o = 0.7$–0.8 and $\phi = 60°$–$80°$ from *NOAA-14*.

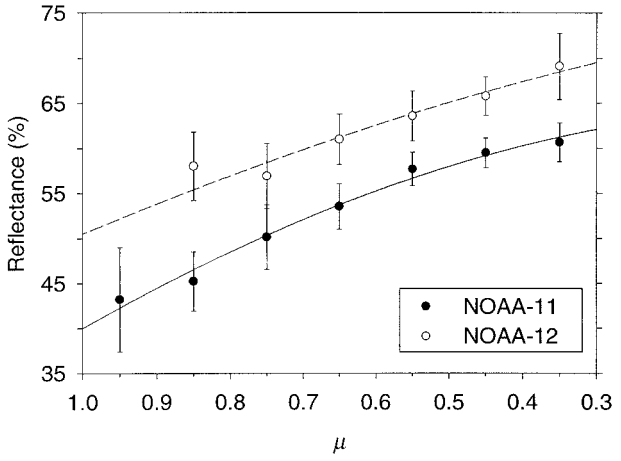

FIG. 6. Mean overcast cloud reflectances and μ at $\mu_o = 0.6$–0.7 and $\phi = 10°$–$30°$ for observations off the coast of California from *NOAA-11* (≈1620 LST) and *NOAA-12* (≈0730 LST).

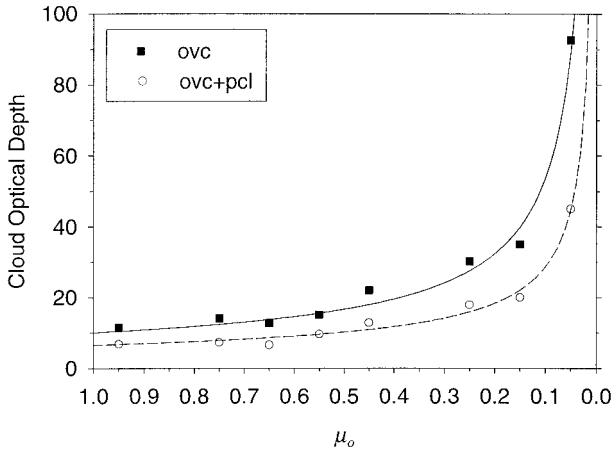

FIG. 7. Mean nadir cloud optical depths and μ_o from *NOAA-11* and *-14* for overcast pixels (''ovc'') and for all cloud-contaminated pixels (''ovc + pcl'').

at nadir, suggest that diurnal effects are likely quite small between 1300 and 1700 LST.

5. Results

a. Cloud optical depth dependence on solar zenith angle

Loeb and Davies (1996) showed that for the general cloud scene, τ_p values inferred from nadir observations suffer from a solar zenith angle dependent bias. In general, cloud optical depths were shown to increase with solar zenith angle for solar zenith angles $\gtrsim 63°$, and at all solar zenith angles when only the thickest (brightest) 10% of the population was considered. Here, the dependence on solar zenith angle is examined using only near-nadir ($\mu > 0.9$) pixels from the afternoon satellites. Figure 7 shows average τ_p ($\langle \tau_p \rangle$) as a function of μ_o when only overcast pixels are considered ''ovc,'' and when all cloud-contaminated pixels are considered ''ovc + pcl.'' Retrievals for the ovc + pcl cases mimic those that would be obtained by ISCCP. A strong systematic increase in $\langle \tau_p \rangle$ with decreasing μ_o occurs, both for the ovc and ovc + pcl cases. While the increase is most pronounced at $\mu_o < 0.3$, it is also noticeable at higher sun elevations. Figure 8 shows the τ_p distributions corresponding to the ovc case. At $\mu_o = 0.9$–1.0, the distribution is quite narrow and peaks at $\tau_p \approx 8$. In contrast, τ_p distributions for the next two μ_o bins are broader and peak at $\tau_p \approx 10$. For $\mu_o < 0.3$, frequency distributions shift toward even larger values with peaks between 13 and 25, and have much longer tails.

The systematic increase in cloud optical depth with solar zenith angle is quite remarkable given that it occurs even in overcast marine stratus layers, which, in principle, should follow plane-parallel radiative transfer theory. A general discussion on possible physical reasons for this systematic increase and its implications is deferred to section 6.

b. Observed versus 1D reflectance as a function of view angle

To reduce the influence of spuriously high values of τ_p, normalization of the 1D calculations at nadir is re-

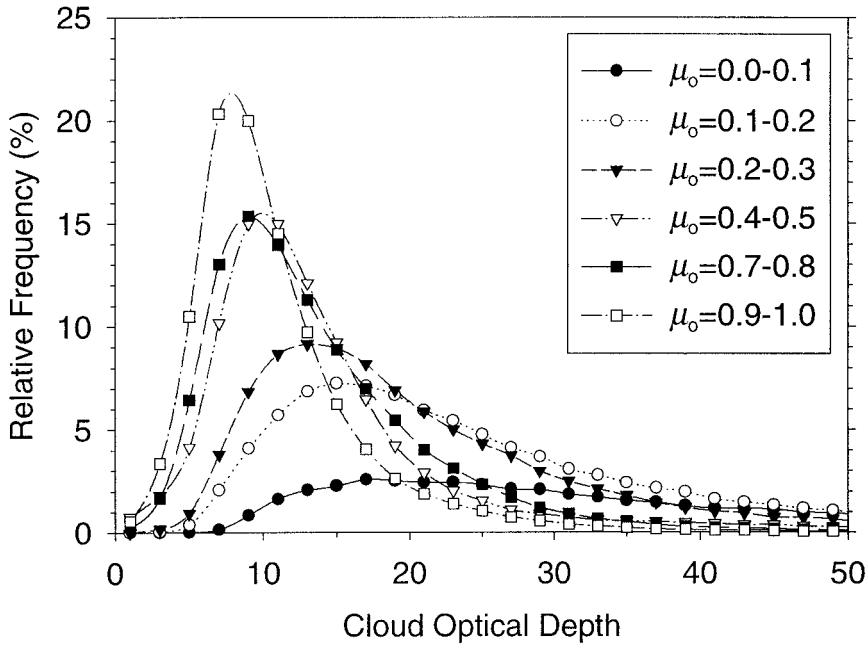

FIG. 8. Cloud optical depth distributions associated with the nadir means in Fig. 7 for the ovc case.

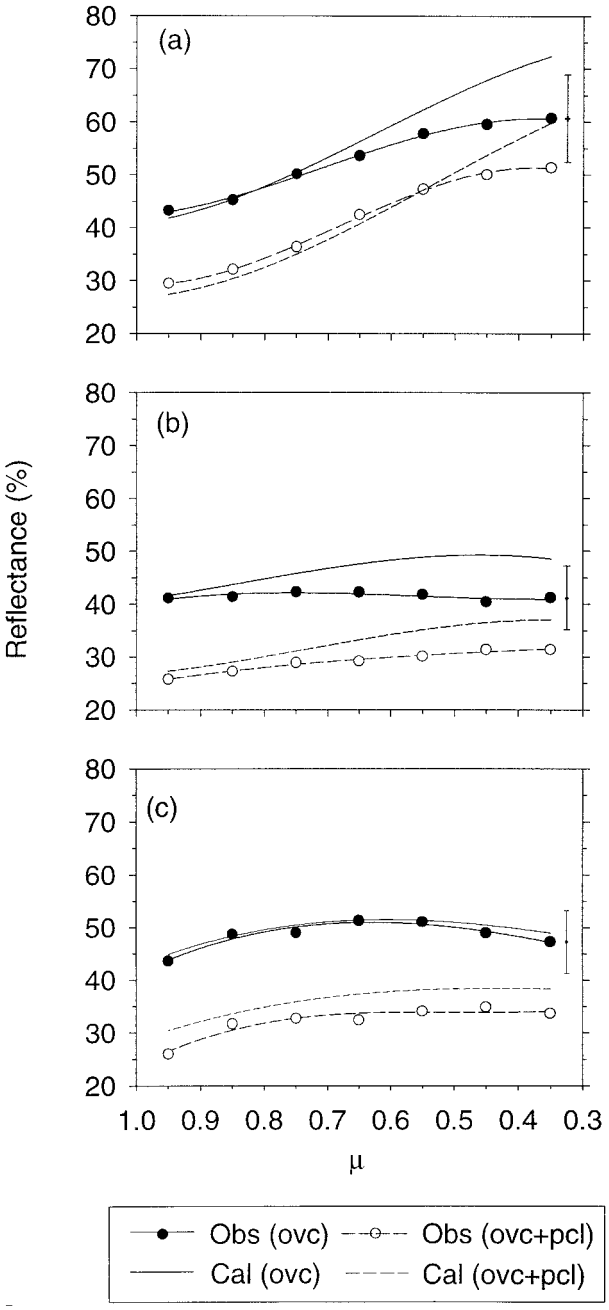

FIG. 9. Observed and calculated mean reflectances and μ for μ_o = 0.6–0.7 at relative azimuth (a) ϕ = 10°–30°; (b) ϕ = 60°–80°; and (c) ϕ = 120°–140°, for *NOAA-11* and *NOAA-14*. Results are shown for overcast pixels (ovc) and for cloud-contaminated pixels (ovc + pcl).

stricted to $\mu_o > 0.6$. Each τ_p value inferred in this range is used to generate 1D reflectances at all combinations of μ_o, μ, and ϕ.

Figure 9 shows observed and calculated mean reflectances for μ_o = 0.6–0.7 in the forward (ϕ = 10°–30°), side (ϕ = 60°–80°), and backward (ϕ = 120°–140°) scattering directions deduced from *NOAA-11* and *NOAA-14* observations. One-dimensional reflectances were derived for r_e = 10 μm and a cloud-top height of 1 km. Error bars account for the standard error in the mean at the 95% significance level plus the relative uncertainty due to pixel area expansion with view angle (Table 3). In the backscattering direction (Fig. 9c), observed and 1D reflectances are in excellent agreement at all μ for the overcast pixel case. In contrast, 1D reflectances increase much more rapidly with decreasing μ than the observed reflectances in the forward- and side-scattering directions, as illustrated in Figs. 9a and 9b. Consequently, the 1D model overestimates observed reflectances by as much as ≈20% (relative difference) at oblique view angles—roughly four times the difference in the backscattering direction. The results are similar for all cloud-contaminated pixels (ovc + pcl). Note that the decrease in observed reflectance relative to 1D values in the backscattering direction for the ''Obs(ovc + pcl)'' case (Fig. 9c) is likely due to a decrease in cloud fraction closer to the coastline.

Interestingly, both the observations and calculations show an increase in anisotropy when all cloud-contaminated pixels are considered (i.e., the ovc + pcl case). The factors responsible for this increase, however, are not the same for the observations and calculations. For the observations, holes or breaks in the cloud field have a larger relative influence in reducing reflectances at nadir than at the limb. At the limb, the greater path length through the clouds and scattering by cloud sides (e.g., Minnis 1989) compensate somewhat for the decrease in reflectance due to the holes. For the 1D calculations, pixels are assumed overcast even when there are subpixel breaks in the cloud field. Consequently, cloud optical depths are made to be much smaller than the actual cloud optical depths when pixels contain broken cloud. Because less multiple scattering occurs in optically thin clouds, the reflectance is more sensitive to the cloud-scattering phase function, which is highly anisotropic. Remarkably, the reflectance anisotropy for the ovc + pcl case is similar for the observations and calculations at this resolution. Consequently, 1D errors caused by the assumption that the pixels are overcast when they contain broken clouds are reduced.

To ensure that results in Fig. 9 also hold for the morning satellite, comparisons are also performed using overcast observations from *NOAA-12*. Figure 10a shows results for μ_o = 0.5–0.6 and ϕ = 10°–30°, and Fig. 10b shows results for μ_o = 0.4–0.5 and ϕ = 150°–170°. Again, the 1D model overestimates observed reflectances in the forward scattering direction and provides a similar μ dependence to that observed in the backscattering direction. Since similar results are obtained both for the afternoon and morning satellites, any possible biases due to changes in cloud cover toward/away from the coastline (section 4b) can thus be discounted as a possible cause for the observed 1D theory differences.

Figure 11 shows reflectances calculated for a wide

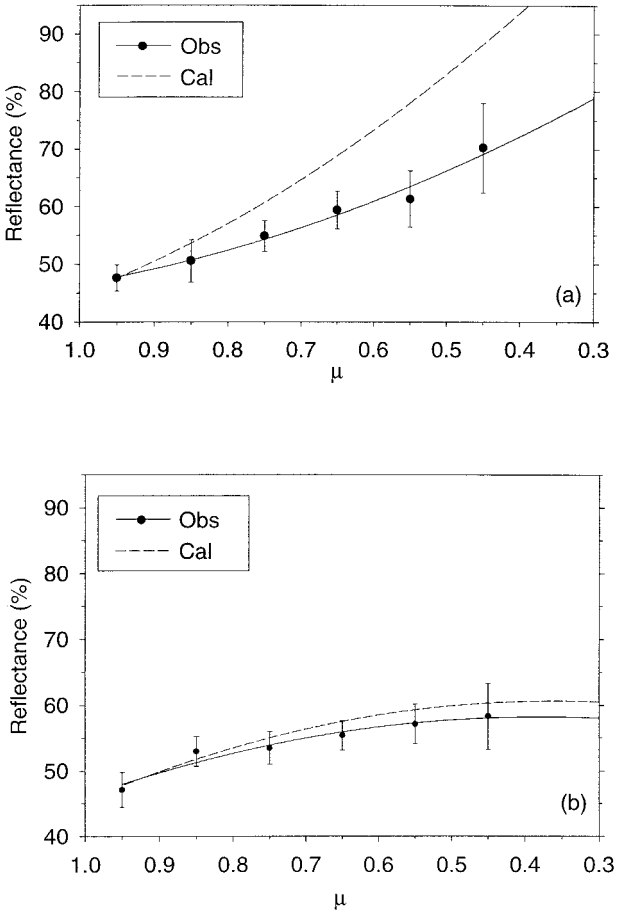

FIG. 10. Observed and calculated mean reflectances and μ for (a) μ_o = 0.5–0.6 and ϕ = 10°–30°; (b) μ_o = 0.4–0.5 and ϕ = 150°–170° for *NOAA-12* ovc pixels.

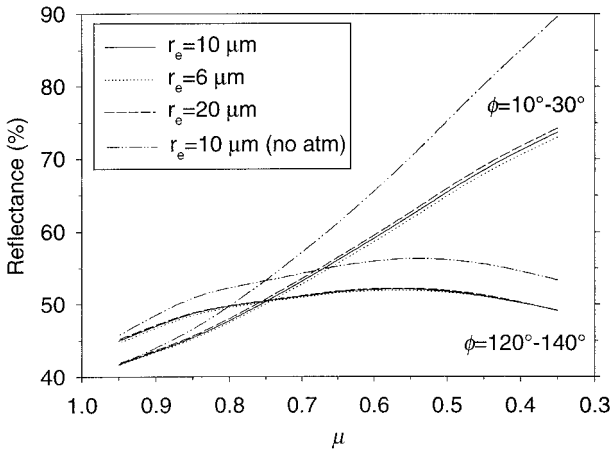

FIG. 11. Reflectances calculated for a wide range of 1D model input assumptions derived using optical depths from overcast nadir observations in the same manner as the Cal (ovc) curves in Fig. 9.

range of 1D model assumptions. The optical depths used in these calculations were derived from the observations at nadir in the same manner as those used to generate the reflectances shown in Fig. 9. Apart from the case in which no atmospheric effects are included ["r_e = 10 μm (No Atm)"], relative differences in 1D reflectance due to drastic changes in cloud microphysics are $\lesssim$2%. The reason for the slight increase in reflectance with r_e in the forward-scattering direction is because the fraction of the incident beam that is scattered into the forward direction and contributes to the reflectance increases with r_e. Also apparent from Fig. 11 is the large sensitivity to ozone absorption and molecular and aerosol scattering in the forward scattering direction. To examine whether changes in the cloud-free atmosphere can cause calculated reflectances to more closely resemble observed values in the forward-scattering direction, simulations were also performed using different concentrations of O_3 and aerosol. When aerosol optical depth is increased by a factor of 3, and the LOWTRAN-7 tropical ozone profile is replaced by the subarctic winter profile (resulting in a 30% relative increase in ozone optical depth), the decrease in reflectance is only $\approx$6% (relative decrease), not sufficient to match observed values.

Figure 12 shows differences in reflectance (observed minus calculated) for overcast pixels from the afternoon satellites as a function of μ and μ_o for the available ϕ bins. The 1D calculations in this comparison correspond to the "r_e = 10 μm" case with a 1-km cloud-top height. Solid lines represent linear fits to all available reflectance differences at $\mu_o > 0.5$ (only a subset of the symbols were plotted for clarity). For $\mu_o > 0.5$, reflectance differences in the backscattering direction (Fig. 12b) are much smaller in magnitude than those in the forward direction (Fig. 12a). From Fig. 12b, 1D reflectances are within $\approx$5% ($\approx$10% relative difference) of observed values. Small relative differences ($\lesssim$5% relative difference) were also observed in the backscattering direction for the morning *NOAA-12* California observations at μ_o = 0.4–0.5 (not shown). The slight decrease in reflectance at small μ in Fig. 12b is likely due to uncertainties in scene identification, as was discussed in section 4a. In contrast, differences in the forward-scattering direction are much larger and show a much stronger μ dependence. For $\mu_o > 0.5$, differences systematically decrease from $\approx$0% at nadir (where the calculations are normalized) to $\approx -10\%$ ($\approx$20% relative difference) at μ = 0.3–0.4. At lower sun elevations, this dependence is even more pronounced; the 1D model underestimates observed reflectances at nadir by more than 5% ($\approx$15% relative difference) but overestimates reflectances at most oblique view angles by $\approx$10%–15% ($\approx$15%–20% relative difference). In the backscattering direction at low sun elevations, the differences are relatively insensitive to μ. A similar result was obtained by Loeb and Davies (1997).

c. Cloud optical depth view angle dependence

1) OVERCAST PIXELS

The discussion thus far has concerned possible biases in reflectance estimates based on 1D theory. Here, these

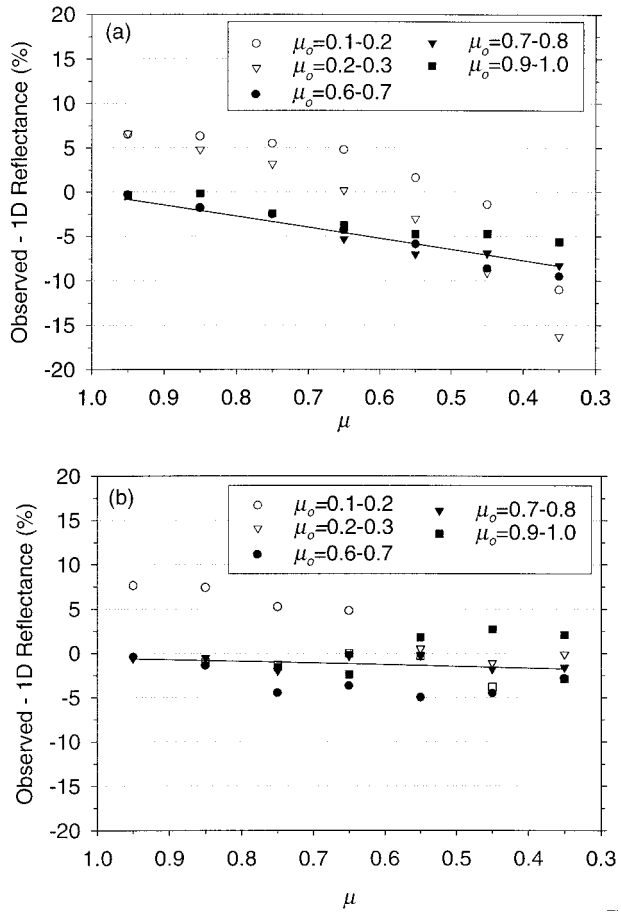

FIG. 12. Differences in reflectance (observed minus calculated) and μ and μ_o for available ϕ bins in (a) the forward- (ϕ = 0°–90°) and (b) backward- (ϕ = 90°–180°) scattering directions for *NOAA-11* and *-14* overcast pixels. The 1D calculations correspond to the "r_e = 10 μm" case with a 1-km cloud-top height. Solid lines represent linear fits to all available reflectance differences at $\mu_o > 0.5$ (only a subset of the symbols are plotted for clarity).

biases are examined in terms of visible wavelength optical depths that are commonly used to characterize cloud properties in both climate models and satellite retrievals.

Figure 13 shows mean cloud optical depths ($\langle\tau_p\rangle$) inferred from separate analyses of the *NOAA-12* and *NOAA-11* and *-14* satellite measurements. In the backscattering direction (Figs. 13b and 13d), cloud optical depths show very little sensitivity to μ—differences in $\langle\tau_p\rangle$ at different μ are well within the range of uncertainty. This lack of sensitivity is even found for μ_o = 0.1–0.2 in Fig. 13b, where $\langle\tau_p\rangle$ at all μ are strongly influenced by the solar zenith angle bias (section 5.1). Cloud optical depths are also relatively insensitive to μ at zenith sun (Fig. 13c, solid triangles). As noted earlier, consistent $\langle\tau_p\rangle$ in different viewing configurations does not necessarily mean that retrievals are accurate in an absolute sense. Absolute accuracy would have to be determined from an independent means (e.g., measurements of droplet sizes, column amounts of water, etc.).

In the forward-scattering direction, a strong systematic decrease in $\langle\tau_p\rangle$ with decreasing μ is obtained at moderate- and low-sun elevations (Figs. 13a and 13c). For example, at μ_o = 0.6–0.7 $\langle\tau_p\rangle$ decreases from ≈14 at nadir to ≈8 at μ = 0.3–0.4. While $\langle\tau_p\rangle$ increases with decreasing μ_o at nadir, Fig. 13c shows that the opposite trend occurs at μ = 0.3–0.4. Consequently, the decrease in $\langle\tau_p\rangle$ with decreasing μ becomes even more pronounced at lower sun elevations.

Note that because of the nonlinear relationship between reflectance and cloud optical depth, the range in $\langle\tau_p\rangle$ at μ = 0.3–0.4 in the forward-scattering direction is much smaller than at nadir. Since reflectance varies roughly linearly with cloud optical depth for thinner clouds and shows a much more gradual (nonlinear) change for thicker clouds, smaller changes in τ_p are required to match the observed reflectances at limb views in the forward scattering direction, on average, than at nadir views, where τ_p may need to be increased well into the nonlinear part of the reflectance-optical depth curve to match the observed reflectances (cf. Loeb and Davies 1996).

Figure 14 shows the relative frequency distributions of τ_p corresponding to the μ_o = 0.6–0.7 case in Figs. 13c and 13d. In the forward-scattering direction (Fig. 14a), there is a systematic shift in the peak of the distribution toward lower τ_p as μ decreases. At the same time, the overall distribution becomes much narrower, implying that standard deviations also decrease with view angle. In contrast, the τ_p distributions in the backscattering direction (Fig. 14b) show very little change with μ. The peak remains fixed at $\tau_p \approx 7$, and the width of the distribution stays fairly constant.

The dependence of cloud optical depth on view angle in the forward-scattering direction is also very sensitive to whether the clouds are optically thin or thick. In Fig. 15, average cloud optical depths for three percentile intervals of τ_p are provided for μ_o = 0.6–0.7 in the forward and backward-scattering directions. Shown are results for thin clouds ("0%–33%"—τ_p lying below the 33rd percentile), moderate clouds ("33%–66%"—τ_p lying between the 33rd and 66th percentiles) and thick clouds ("66%–99%"—τ_p lying between the 66th and 99th percentiles). As clouds become optically thicker, the tendency for cloud optical depth to decrease with decreasing μ in the forward direction becomes more pronounced. In the backscattering direction, a slight decrease in τ_p with decreasing μ is observed for thin and moderately thick clouds, but this decrease is much smaller than in the forward direction and is not apparent for the thickest clouds (66%–99%). Figure 16 shows similar results for μ_o = 0.9–1.0 and μ_o = 0.2–0.3 in the forward-scattering direction only (sample sizes in the backscattering direction were too small to stratify by optical depth ranges). At zenith sun (Fig. 16a), virtually no μ dependence in cloud optical depth is detected for any of the thickness

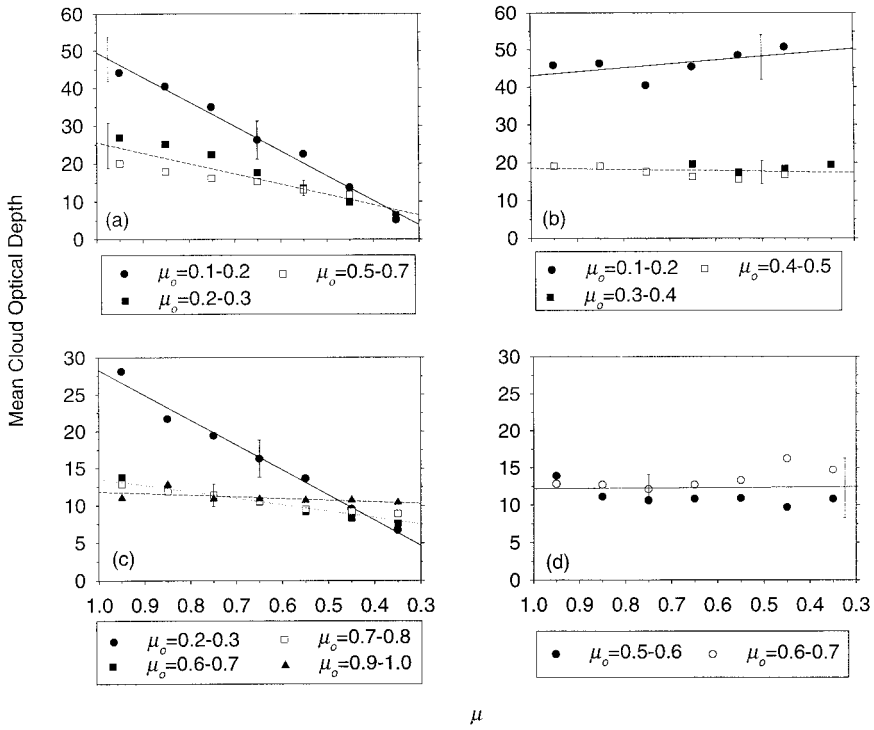

FIG. 13. Mean cloud optical depths and μ for a range of μ_o for overcast pixels. (a) *NOAA-12* in the forward-scattering direction; (b) *NOAA-12* in the backward-scattering direction; (c) *NOAA-11* and *-14* in the forward-scattering direction; and (d) *NOAA-11* and *-14* in the backward-scattering direction.

classes. At low sun (Fig. 16b), a very strong view angle dependence is observed, especially for the thickest clouds.

2) OVERCAST AND PARTLY CLOUDY PIXELS

Figure 17 shows the μ dependence of $\langle \tau_p \rangle$ for all cloud-contaminated pixels (i.e., partly cloudy and overcast pixels), under the (erroneous) assumption that all pixels are completely cloud covered. This approach mimics the type of approach used by ISCCP. Only the morning and afternoon retrievals in the forward direction are shown, since results in the backscattering direction are qualitatively very similar to those in Fig. 13. The results in Fig. 17 indicate that when all cloud-contaminated pixels are considered, $\langle \tau_p \rangle$ values at nadir are lower than those for the overcast pixels alone (Fig. 13) by a factor of $\approx$2. As a result, the overall view angle bias in average reflectance is similar to that for the thinnest 33% of the overcast cloud population shown in Figs. 15 and 16 (for the afternoon orbits). Thus, while $\langle \tau_p \rangle$ for the overcast case at moderate sun elevations decreases from $\approx$14 at nadir to $\approx$8 at the limb ($\approx$42% relative decrease), the drop is much smaller for the general (overcast + broken) cloud case, decreasing from $\approx$6 at nadir to $\approx$4.5 at the limb ($\approx$25% relative decrease).

d. Albedo view angle dependence

Figure 18 shows mean TOA visible albedo derived from optical depths for the forward-, side-, and backscattering directions when only overcast pixels are considered. In the forward-scattering direction, a rather dramatic decrease in TOA albedo from $\approx$50% at nadir to $\approx$40% at $\mu = 0.35$ (i.e., a relative decrease of $\approx$20%) is obtained. This decrease is associated with the $\approx$42% relative decrease in $\langle \tau_p \rangle$ mentioned in section 5c1. In the backscattering direction, cloud albedo remains fairly constant (to within $\approx$5%) and does not show any systematic μ dependence.

It was noted in section 5c2 that when all cloud-contaminated pixels are assumed overcast, the magnitude of the $\langle \tau_p \rangle$ bias is much smaller than when only overcast pixels are considered ($\approx$25% compared to 42%). However, owing to the nonlinear dependence of albedo on cloud optical depth, the relative decrease in TOA albedo between nadir and $\mu = 0.35$ for these two cases is comparable. For the overcast case, the relative decrease in TOA albedo is $\approx$20%, compared to $\approx$15% when all cloud-contaminated pixels are considered. Thus, while the $\langle \tau_p \rangle$ dependence on μ is smaller for thinner (or broken) clouds—making it more difficult to detect—the error in TOA albedo remains sizable. Since ISCCP cloud optical depth retrievals are also based on the as-

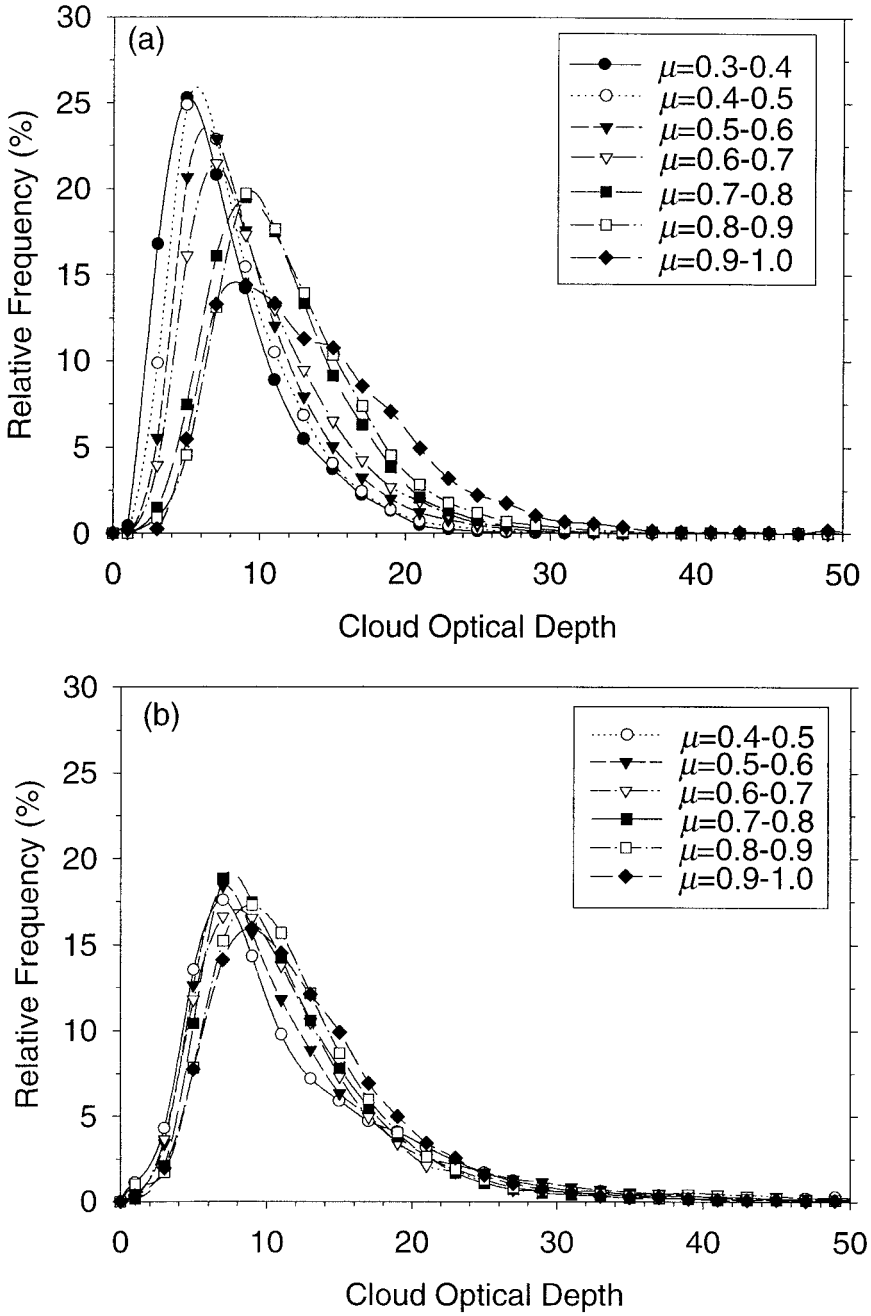

FIG. 14. Relative frequency distributions at different μ for μ_o = 0.6–0.7 and (a) ϕ = 10°–30°; and (b) ϕ = 120°–140°. *NOAA-11* and *-14* overcast observations are shown.

sumption that all cloud-contaminated pixels are overcast, cloud albedos inferred from ISCCP likely suffer from similar biases.

6. Discussion

Results in the present study are in qualitative agreement with other studies. As mentioned earlier, Loeb and Davies (1996) also found a substantial increase in cloud optical depth with solar zenith angle. In another study, Loeb and Davies (1997) showed that 1D reflectances increase more rapidly with view angle than the observed reflectances in the forward-scattering direction at low-sun elevations but show a similar μ dependence in the backward direction. Note that these studies involved measurements from many different cloud types (all non-cirrus clouds over the tropical oceans between 30°N and 30°S) and were inferred from ERBE scanner observa-

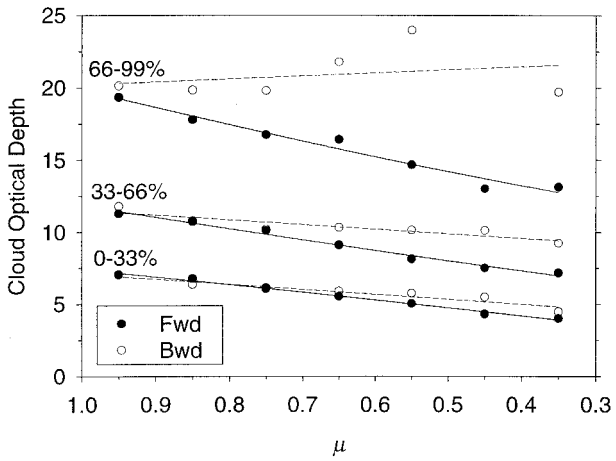

FIG. 15. Average cloud optical depths for optically thin, moderate, and thick clouds and μ for μ_o = 0.6–0.7 in the forward- and backward-scattering directions. Each point is an average value over a specific percentile interval range (or cloud thickness class): 0%–33% (thin), 33%–66% (moderate), or 66%–99% (thick). The averages were derived from the relative frequency distributions in Fig. 14.

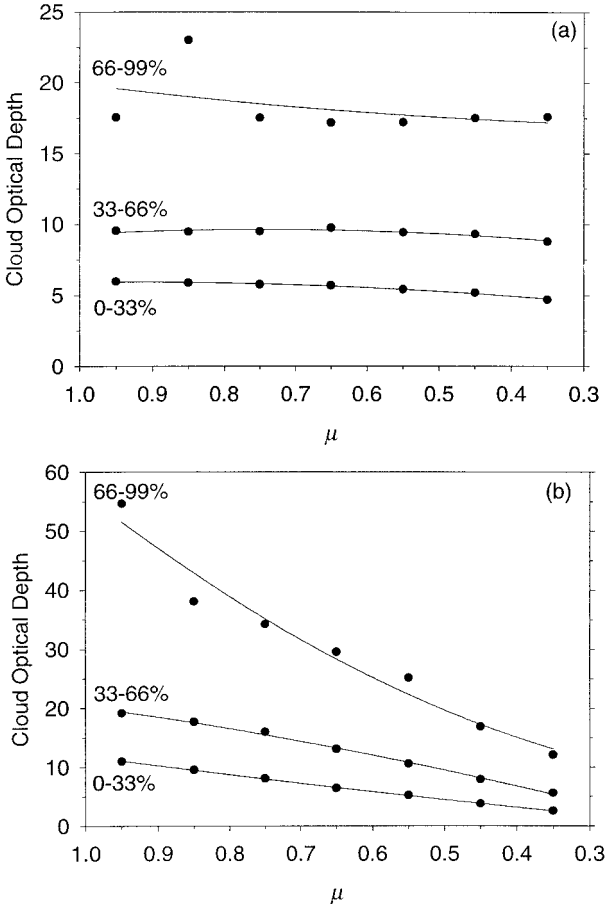

FIG. 16. Average cloud optical depths corresponding to optically thin, moderate, and thick clouds and μ for (a) μ_o = 0.9–1.0 and (b) μ_o = 0.2–0.3 in the forward-scattering direction. *NOAA-11* and *-14* overcast observations are shown.

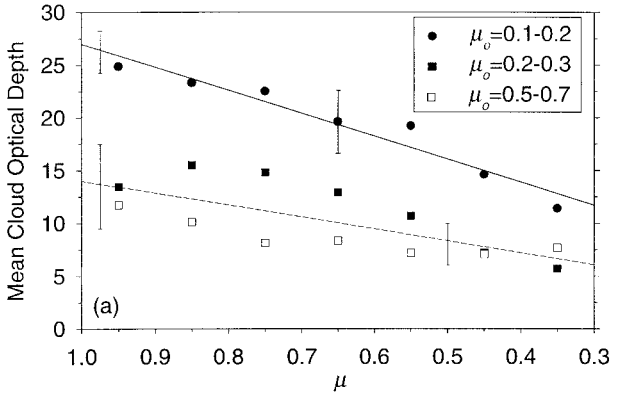

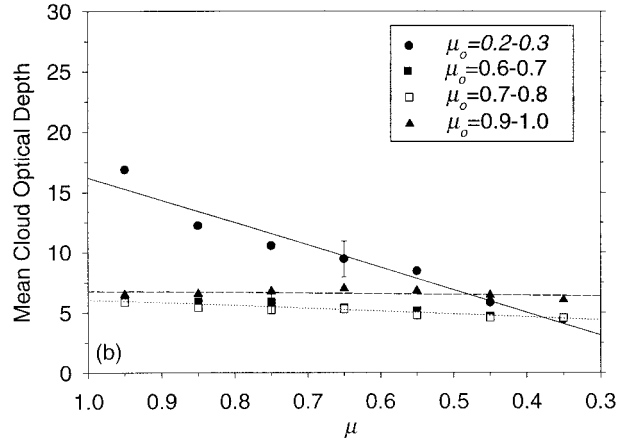

FIG. 17. Average cloud optical depths and μ for the forward-scattering direction and various μ_o bins for cloud-contaminated pixels. (a) *NOAA-12* and (b) *NOAA-11* and *-14*.

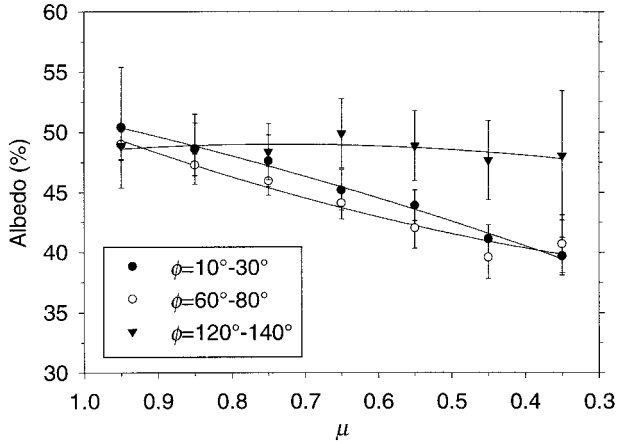

FIG. 18. Mean TOA albedo (%) and μ at ϕ = 10°–30°, ϕ = 60°–80° and ϕ = 120°–140° for the *NOAA-11* and *-14* ovc cases.

tions which are broadband and have a low spatial resolution ($\approx 31 \times 47$ km^2 at nadir). The remarkable similarities between observed-1D model biases inferred from the Loeb and Davies studies and the present study—in spite of the very different instruments used and cloud types considered—demonstrates that these biases are extremely persistent. That is, they are observed regardless of spectral and spatial resolution (at least above 4 km) and cloud type (except perhaps cirrus). Stuhlmann et al. (1985) compared cloud anisotropic functions (i.e., ratio of Lambertian flux to actual flux) inferred from low-level overcast cloud models developed by Taylor and Stowe (1983) from *Nimbus-7* ERB scanner measurements with plane-parallel calculations for a single cloud optical depth of 20 and cloud-top height of 3 km. The largest differences in the anisotropy of reflected radiation occurred in the forward-scattering direction with 1D reflectances exceeding observed values. Differences also increased with view and solar zenith angle. On the other hand, Rossow (1989) did not find any significant biases. That study compared τ_p retrievals obtained using collocated, simultaneous measurements of cloudy and clear scenes from *GOES-5* (East) and *Meteosat-2* (see Fig. 5 of that study). Unfortunately, those comparisons were not stratified by relative azimuth angle, solar zenith angle, or cloud optical depth and included a considerable number of land scenes as well as oceanic scenes (this alone caused a noticeable sampling bias in the visible radiances). Consequently, the resulting variances in the cloud optical depth differences masked any differences that might have been due to 1D model biases.

More recently, Oreopoulos and Davies (1998) used 3 months of *NOAA-11* Local Area Coverage (LAC) AVHRR observations over the Atlantic Ocean to investigate whether the ''plane-parallel albedo bias'' of Cahalan et al. (1994) estimated from satellite measurements depends on viewing geometry. The average variance in the logarithm of τ_p, which determines the magnitude of the plane-parallel albedo bias, was shown to decrease substantially with increasing view angle in the forward-scattering direction but showed no systematic dependence in the backward direction. These results are consistent with the narrowing in the τ_p frequency distribution with increasing view angle in the forward direction (and thus a decrease in the variance of τ_p) and the small change in the backward direction shown in Fig. 14. Oreopoulos and Davies (1998) also obtained substantially larger variances in the logarithm of τ_p at low-sun elevations consistent with results in Fig. 8.

Of all the clouds, marine stratus are expected to be closest to satisfying the plane-parallel model assumption, given their relatively low aspect ratios and high spatial uniformity. That they fail to comply with plane-parallel theory is quite remarkable. Loeb et al. (1997) showed theoretically, however, that even reflectances from overcast clouds can deviate from 1D theory. They performed Monte Carlo simulations to directly compare

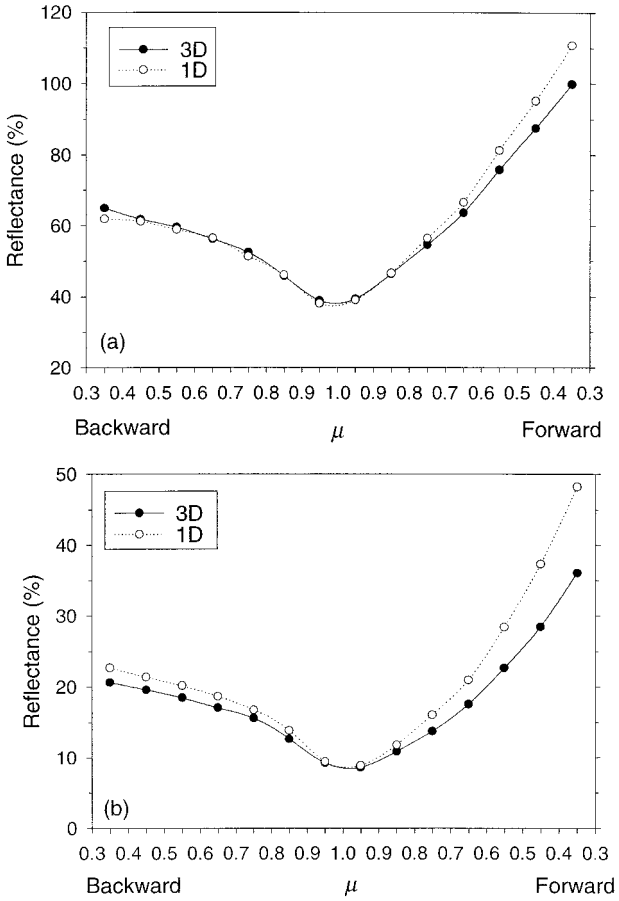

FIG. 19. Monte Carlo model simulations of 3D and 1D reflectances and μ for overcast cloud fields with single scattering albedos (ω_o) of (a) 1.0 and (b) 0.9.

the nadir reflectance dependence on solar zenith angle from 3D and 1D cloud fields for a range of cloud fields. In general, they found that the two most important factors responsible for deviations from 1D theory are cloud-side illumination (for broken cloud fields), and cloud-top structure (i.e., nonflat cloud tops).

To examine how 3D cloud effects influence the reflectance dependence on view angle in overcast conditions, Fig. 19 shows results from Monte Carlo simulations comparing 3D and 1D reflectances from overcast cloud fields with single scattering albedos (ω_o) of 1 and 0.9, respectively. These simulations were generated using the Monte Carlo model of Várnai (1996). In that model, cloud fields are represented by a stochastic, isotropic, and scale-invariant formulation based on Barker and Davies (1992). The 3D cloud field used to produce the results in Fig. 19 is overcast over a (4.4-km)^2 domain and has a variable cloud-top height (with a height standard deviation of $\approx$90 m), a constant visible extinction coefficient of 30 km^{-1} throughout, and a domain average vertical cloud optical depth of 10. The 1D calculations are performed using $\tau_p = 10$. Results are

provided for $\theta_o = 65°$ at different viewing angles in the forward- ($\phi = 30°$–$60°$) and backward- ($\phi = 120°$–$150°$) scattering directions. The largest differences between 1D and 3D reflectances occur in the forward-scattering direction at oblique view angles, consistent with the observations. While a more detailed analysis is deferred to Loeb et al. (1998, manuscript submitted to *J. Atmos. Sci.*) (who also consider the effect of subpixel scale variations in cloud extinction), these results support the hypothesis that horizontal inhomogeneities (bumps on the cloud top) may be responsible for the differences between observations and plane-parallel model calculations. Interestingly, when absorption is included, Fig. 19b shows that the differences between 3D and 1D reflectances become even larger. Thus, 1D retrievals of effective radius from absorbing channels (e.g., 3.7 μm) may also suffer from a view angle dependent bias. In this case, r_e would likely increase with view angle in the forward scattering direction. Preliminary analyses involving 1 month of *NOAA-11* AVHRR observations over the Pacific Ocean (20°–40°S) appear to support this hypothesis (F. L. Chang 1996, personal communication). Consequently, parameterizations and retrievals of cloud liquid water path inferred from visible, 3.7- and 11-μm measurements may also suffer from substantial systematic biases.

7. Summary and conclusions

The plane-parallel model assumption, which assumes clouds to be one-dimensional and therefore horizontally invariant, leads to substantial errors when used to infer cloud optical depth from actual satellite measurements. Direct comparisons between observed reflectances—drawn from extensive marine stratus layers—and plane-parallel model calculations show that 1D theory fails to adequately represent the angular dependence in observed reflectance under certain conditions. Consequently, when 1D models are used to infer cloud properties directly from satellite observations, the retrieved properties exhibit large systematic shifts with changes in viewing geometry. This result is quite remarkable given that it is based on observations of marine stratus—arguably, the closest to plane-parallel in nature.

When inferred on a pixel-by-pixel basis, nadir-derived cloud optical depths show a systematic increase with increasing solar zenith angle, both for overcast and broken marine stratus layers. This finding is consistent with results from an earlier study (Loeb and Davies 1996) which first detected this bias for the general cloud scene using coarse-resolution broadband satellite measurements (ERBE scanner data). When 1D reflectances are directly compared with observations at different view angles, relative differences are generally small ($\lesssim$10% relative difference) in the backscattering direction for solar zenith angles $\lesssim 60°$. In contrast, 1D model reflectances increase much more rapidly with view angle than the observations in the forward-scattering direction. Relative differences at oblique view angles in the forward-scattering direction are $\approx$2–3 times larger than those in the backscattering direction. At solar zenith angles $\gtrsim 60°$, differences in the forward-scattering direction are even larger: the 1D model underestimates observed reflectances at nadir by 20%–30% and overestimates reflectances at the most oblique view angles by 15%–20%.

Observed reflectances are generally more anisotropic when all cloud-contaminated pixels (i.e., both broken and overcast) are included than when only overcast pixels are considered. Interestingly, 1D calculations which assume that all pixels (including partly cloudy pixels) are completely cloud covered also show an increase in anisotropy but for a different reason. For partly cloudy pixels, 1D clouds have lower optical depths (due to the assumption that pixels are overcast), and therefore reflectances are more sensitive to the cloud-scattering phase function, which is highly anisotropic. Consequently, 1D errors caused by the assumption that partly cloudy pixels completely fill the sensor field-of-view are reduced.

One-dimensional retrievals of cloud optical depth are fairly insensitive to changes in view angle in the backscattering direction. Both the mean cloud optical depths and the underlying optical depth frequency distributions show no appreciable change with view angle in the backscattering direction. In the forward-scattering direction, mean cloud optical depths decrease by as much as $\approx$40% between nadir and oblique view angles. Cloud optical depth frequency distributions in the forward-scattering direction show a steady shift toward lower optical depths with increasing view angle and a narrowing in the width of the distribution. For thinner clouds, and for broken clouds in which the pixels are assumed to be completely overcast, absolute differences in τ_p between nadir and limb views are smaller because reflectance varies approximately linearly with cloud optical depth. Thus, in the case of broken marine stratocumulus, the common practice of assuming that pixels are overcast (as is done for ISCCP) when they are not mitigates to some extent the bias thereby confounding its detection. Nevertheless, when distributions of τ_p are used to generate mean TOA albedos, a significant dependence on viewing geometry is observed, regardless of whether clouds are broken or overcast. In the forward direction, mean TOA albedos decrease by as much as 15%–20% (relative decrease) between nadir and the most oblique viewing angle. In the backscattering direction, variations in albedo are $\lesssim$5% (relative difference).

The results presented here demonstrate that the common practice of using plane-parallel theory to retrieve cloud properties, even for clouds that are arguably plane-parallel in appearance, is flawed and leads to significant biases in retrieved cloud products. Since the biases tend to be less pronounced in the backscattering direction at solar zenith angles $\lesssim 60°$, it is recommended

that application of 1D theory be restricted to those angles.

Based on Monte Carlo simulations presented here, and in earlier studies, 3D cloud effects are the likely cause for the discrepancies between observed radiances and radiances calculated on the basis of 1D theory. In particular, cloud-top structure (e.g., bumps on cloud tops), which can cause enhanced reflectivities at nadir views (Loeb et al. 1997) and cloud shadowing in the forward direction (Wendling 1977; Davies 1984; Barker 1994; Loeb et al. 1998, manuscript submitted to *J. Atmos. Sci.*), may have substantial effects even for marine stratus. Clearly further research is needed.

Acknowledgments. The authors would like to thank Tamás Várnai for making his Monte Carlo model code available. This research was supported by NASA Grant NAG 11263.

REFERENCES

Barker, H. W., 1994: Solar radiative transfer for wind-sheared cumulus cloud fields. *J. Atmos. Sci.,* **51,** 1141–1156.

——, and J. A. Davies, 1992: Solar radiative fluxes for stochastic, scale-invariant broken cloud fields. *J. Atmos. Sci.,* **49,** 1115–1126.

Bohren, C. F., and D. R. Huffman, 1983: *Absorption and Scattering of Light by Small Particles.* John Wiley, 530 pp.

Bréon, F.-M., 1992: Reflectance of broken cloud fields: Simulation and parameterization. *J. Atmos. Sci.,* **49,** 1221–1232.

Busygin, V. P., N. A. Yevstratov, and Y. M. Feigel'son, 1973: Optical properties of cumulus clouds, and radiant fluxes for cumulus cloud cover (English translation). *Izv. Acad. Sci. USSR, Atmos. Oceanic Phys.,* **9,** 1142–1151.

Cahalan, R. F., W. Ridgway, W. J. Wiscombe, T. L. Bell, and J. B. Snider, 1994: The albedo of fractal stratocumulus clouds. *J. Atmos. Sci.,* **51,** 2434–2455.

Coakley, J. A., Jr., 1991: Reflectivities of uniform and broken layered clouds. *Tellus,* **43B,** 420–433.

——, and F. P. Bretherton, 1982: Cloud cover from high-resolution scanner data: Detecting and allowing for partially filled fields of view. *J. Geophys. Res.,* **87,** 4917–4932.

——, and D. G. Baldwin, 1984: Toward the objective analysis of clouds from satellite imagery data. *J. Climate Appl. Meteor.,* **23,** 721–730.

——, and R. Davies, 1986: The effect of cloud sides on reflected solar radiation as deduced from satellite observations. *J. Atmos. Sci.,* **43,** 1025–1035.

Davies, R., 1978: The effect of finite geometry on the three-dimensional transfer of solar irradiance in clouds. *J. Atmos. Sci.,* **35,** 1712–1725.

——, 1984: Reflected solar radiances from broken cloud scenes and the interpretation of scanner measurements. *J. Geophys. Res.,* **89,** 1259–1266.

——, 1994: Spatial autocorrelation of radiation measured by the Earth Radiation Budget Experiment: Scene inhomogeneity and reciprocity violation. *J. Geophys. Res.,* **99,** 20 879–20 887.

Deirmendjian, D., 1969: *Electromagnetic Scattering on Spherical Polydispersions.* Elsevier, 290 pp.

Di Girolamo, L., and R. Davies, 1997: Cloud fraction errors caused by finite resolution measurements. *J. Geophys. Res.,* **102,** 1739–1756.

Frulla, L. A., J. A. Milovich, and D. A. Gagliardini, 1995: Illumination and observation geometry for NOAA-AVHRR images. *Int. J. Remote Sens.,* **16,** 2233–2253.

Hale, G. M., and M. R. Querry, 1973: Optical constants of water in the 200-nm to 200-μm wavelength region. *Appl. Opt.,* **12,** 555–563.

Kidwell, K. B., 1994: NOAA polar orbiter data users guide. U.S. Department of Commerce, National Oceanic and Atmospheric Administration, National Environmental Satellite, Data and Information Service, National Climatic Data Center, Satellite Data Services Division, 250 pp. [Available from Federal Office Building #3, Room G-233, Washington, DC 20233.]

Klein, S. A., and D. L. Hartmann, 1993: The seasonal cycle of low stratiform clouds. *J. Climate,* **6,** 1587–1606.

Kneizys, F. X., E. P. Shettle, L. W. Abreu, J. H. Chetwynd Jr., G. P. Anderson, W. O. Gallery, J. E. A. Selby, and S. A. Clough, 1988: Users guide to LOWTRAN 7. Rep. AFGL–TR–88–0177, 137 pp. [Available from Phillips Laboratory, Geophysics Directorate, PL/GPOS, 29 Randolph Rd., Hanscom AFB, MA 01731-3010.]

Kobayashi, T., 1993: Effects due to cloud geometry on biases in the albedo derived from radiance measurements. *J. Climate,* **6,** 120–128.

Loeb, N. G., 1997: In-flight calibration of NOAA AVHRR visible and near-IR bands over Greenland and Antarctica. *Int. J. Remote Sens.,* **18,** 477–490.

——, and R. Davies, 1996: Observational evidence of plane parallel model biases: Apparent dependence of cloud optical depth on solar zenith angle. *J. Geophys. Res.,* **101,** 1621–1634.

——, and ——, 1997: Angular dependence of observed reflectances: A comparison with plane parallel theory. *J. Geophys. Res.,* **102,** 6865–6881.

——, T. Várnai, and R. Davies, 1997: The effect of cloud inhomogeneities on the solar zenith angle dependence of nadir reflectance. *J. Geophys. Res.,* **102,** 9387–9395.

McKee, T. B., and S. K. Cox, 1974: Scattering of visible radiation by finite clouds. *J. Atmos. Sci.,* **31,** 1885–1892.

Minnis, P., 1989: Viewing zenith angle dependence of cloudiness determined from coincident GOES East and GOES West data. *J. Geophys. Res.,* **94,** 2303–2320.

——, and E. F. Harrison, 1984: Diurnal variability of regional cloud and clear-sky radiative parameters derived from GOES data. Part II: November 1978 cloud distributions. *J. Climate Appl. Meteor.,* **23,** 1012–1051.

——, P. W. Heck, D. F. Young, C. W. Fairall, and J. B. Snider, 1992: Stratocumulus cloud properties derived from simultaneous satellite and island-based instrumentation during FIRE. *J. Appl. Meteor.,* **31,** 317–339.

Oreopoulos, L., and R. Davies, 1998: Plane parallel albedo biases from satellite observations. Part I: Dependence on resolution and other factors. *J. Climate,* in press.

Rossow, W. B., 1989: Measuring cloud properties from space: A review. *J. Climate,* **2,** 201–213.

——, L. C. Garder, and A. A. Lacis, 1989: Global, seasonal cloud variations from satellite radiance measurements. Part I: Sensitivity of analysis. *J. Climate,* **2,** 419–458.

Shenk, W. F., and V. V. Salomonson, 1972: A simulation study exploring the effects of sensor spatial resolution on estimates of cloud cover from satellites. *J. Appl. Meteor.,* **11,** 214–220.

Singh, S. M., and A. P. Cracknell, 1986: The atmospheric effects for SPOT using AVHRR channel-1 data. *Int. J. Remote Sens.,* **7,** 361–377.

Sprent, P., 1989: *Applied Nonparametric Statistical Methods.* Chapman and Hall Limited, 259 pp.

Stamnes, K., S.-C. Tsay, W. Wiscombe, and K. Jayaweera, 1988: Numerically stable algorithm for discrete-ordinate-method radiative transfer in multiple scattering and emitting layered media. *Appl. Opt.,* **24,** 2502–2509.

Stuhlmann, R., P. Minnis, and G. L. Smith, 1985: Cloud bidirectional reflectance functions: A comparison of experimental and theoretical results. *Appl. Opt.,* **24,** 396–401.

Taylor, V. R., and L. L. Stowe, 1983: Reflectance characteristics of uniform earth and cloud surfaces derived from Nimbus 7 ERB. *J. Geophys. Res.,* **89,** 4987–4996.

Várnai, T., 1996: Reflection of solar radiation by inhomogeneous

clouds. Ph.D. thesis, McGill University, 146 pp. [Available from McGill University, 805 Sherbrooke Street West, Montreal, PQ, H3A 2K6 Canada.]

Warren, S. G., C. J. Hahn, J. London, R. M. Chervin, and R. L. Jenne, 1988: Global distribution of total cloud cover and cloud type amounts over the ocean. NCAR Tech. Note TN-317+STR, Boulder, CO, 42 pp. plus 170 maps.

Wendling, P., 1977: Albedo and reflected radiance of horizontally inhomogeneous clouds. *J. Atmos. Sci.*, **34,** 642–650.

Wielicki, B. A., and R. M. Welch, 1986: Cumulus cloud properties derived using Landsat satellite data. *J. Climate Appl. Meteor.*, **25,** 261–276.

——, and L. Parker, 1992: On the determination of cloud cover from satellite sensors: The effect of sensor spatial resolution. *J. Geophys. Res.*, **97,** 12 799–12 823.

Ye, Q., and J. A. Coakley Jr., 1996: Biases in earth radiation budget observations. Part 2: Consistent scene identification and anisotropic factors. *J. Geophys. Res.*, **101,** 21 253–21 263.